PCCP

ROYAL SOCIETY OF CHEMISTRY

PAPER

View Article Online
View Journal | View Issue

Cite this: *Phys. Chem. Chem. Phys.*, 2026, **28**, 6717

From high loading to high activity: unraveling the correlation in high-performance single-atom catalyst design

Degao Zhang,[a] Qian Lin,[a] Guangjun Nan,[b] Yi Zhang,[a] Dawei Fu[a] and Liyan Xie *[a]

Single-atom catalysts (SACs) have shown great promise for electrocatalytic applications such as the oxygen evolution reaction (OER). However, the high surface free energy of the isolated metal sites in SACs results in a generally low metal loading, which limits the density of active sites. Herein, we constructed low- and high-loading SACs on a γ-graphyne (GY) support using a series of transition metals (Fe, Co, Ni, Cu, Rh, Pd, Ag, Ir, and Pt) to study their OER performance. Calculations demonstrate that a high metal loading reduces the OER overpotential of Fe- and Co-GY catalysts, especially for Fe-GY, which shows exceptional activity with an overpotential of only 0.39 V. Notably, the bonding and anti-bonding stabilized energy difference (BASED) analysis indicates that the high loading Fe-GY optimizes the binding strength of *OH and *O intermediates, thereby lowering the overpotential of the rate-determining step (*OH → *O). This change is attributed to the synergy between adjacent Fe atoms, which modifies the charge distribution at the Fe sites, as shown by differential charge and density of states (DOS) analyses. Our findings help pave the way for the rational design of high-loading SACs for electrocatalysis.

Received 4th January 2026,
Accepted 11th February 2026

DOI: 10.1039/d6cp00014b

rsc.li/pccp

Introduction

Single-atom catalysts (SACs) have garnered extensive attention in key electrochemical reactions due to maximizing atom utilization and superior activity,[1,2] such as the oxygen reduction reaction (ORR),[3] oxygen evolution reaction (OER),[4,5] hydrogen evolution reaction (HER),[6] and CO_2 conversion.[7,8] However, the high surface free energy and thermal instability of the isolated metal sites in SACs make them prone to agglomeration into clusters, which typically leads to low metal loading.[9,10] Consequently, the low density of active sites results in inadequate overall catalytic activity and hinders their practical deployment. In particular, higher metal loadings in SACs enable thinner catalyst layers in polymer–electrolyte–membrane (PEM) systems, reducing material cost, improving mass transport, and ultimately enhancing system cost-performance.[11] Therefore, achieving high metal loading in SACs is crucial for practical applications, driving extensive research in this area. For example, Gong and coworkers reported a dry-solid-electrochemical synthesis (DSES) technique for the scalable, energy-efficient production of high-loading SACs on pure carbon supports, achieving record metal contents (*e.g.*, Pt up to 35.0 wt%).[12]

Meanwhile, advanced characterization techniques have provided evidence that adjacent sites of SACs exert a mutual influence as the loading density increases. For instance, Li *et al.* investigated the chemical configuration and local coordination environment of the Fe-SAC material using X-ray absorption spectroscopy (XAS). They observed a shift of the absorption edge toward lower energy with increasing density of Fe sites, revealing a higher electron density at the Fe sites in high-loading Fe-SACs.[13] Furthermore, the close proximity of metal centers in high-loading SACs also enables "cooperative catalysis".[14] Thus, given the critical nature of the interactions between adjacent sites in SACs, understanding the fundamental principles is important for the rational design of high-loading SACs.

Complementing the experimental findings, theoretical calculations, such as density functional theory (DFT), were also employed in the study of high-loading SACs to elucidate the interactions between the active sites from an atomic perspective. For example, Jin *et al.* investigated the interactions between cobalt sites in densely populated Co SACs on N- and O-doped graphene matrix using DFT calculations. Studies have shown that in densely populated Co SACs, the electronic structure of cobalt atoms changes through charge redistribution, leading to a reduced Bader charge and an elevated d-band center, which facilitates the activation of reactants during the

[a] *Institute for Science and Applications of Molecular Ferroelectrics, Key Laboratory of the Ministry of Education for Advanced Catalysis Materials, Zhejiang Normal University, Jinhua, 321004, P. R. China. E-mail: liyanxie@zjnu.edu.cn*
[b] *Department of Physics, Zhejiang Normal University, Jinhua, Zhejiang 321004, P. R. China*

trans-stilbene epoxidation.[15] Jin and coworkers calculated the magnetic moments of adjacent Fe–N_4 sites at varying distances (d_{site}) in graphene to investigate the influence of iron loading density on the oxygen reduction reaction (ORR) catalytic activity. The calculations show that when d_{site} values are below 1.6 nm, increased filling of partially occupied d orbitals causes a significant reduction in spin moment, thereby preventing strong adsorption of OH intermediates during the ORR.[16] Evidently, theoretical calculations offer unique advantages for understanding the adjacent site interactions in high-loading SACs.

Recently, Wu *et al.* reported γ-graphyne (GY), a novel two-dimensional carbon allotrope.[17] Its structure features both hexagonal carbon rings and acetylene bonds, formed by sp- and sp^2-hybridized carbon atoms. In addition, He and colleagues calculated the adsorption energies of several transition metal (TM) atoms on graphene (Fig. S1) and GY (Fig. 1a). Their results indicated that TM adsorption is more stable on GY, attributable to the presence of sp-hybridized carbon atoms in its structure.[18] Therefore, GY promises to be a suitable support material for synthesizing high-loading SACs. Although previous theoretical studies have established the OER performance of TM-doped GY (TM-GY) systems, research studies on high-loading TM-GY and the interactions between TM sites remain scarce.[19,20]

Thereby, we systematically calculated and compared the OER activities of both low- and high-loading TM-GY systems (Fig. 1, where TM = Fe, Co, Ni, Cu, Rh, Pd, Ag, Ir, and Pt), aiming to elucidate the influence of metal loading on catalytic performance. Our results demonstrate that, relative to low loading conditions, high loading reduces the overpotential in Fe-, Co-, and Cu-GY catalysts while exerting nearly negligible effects on other TM-GY systems. Stability concerns preclude the inclusion of Pd-GY and Ag-GY systems in the current analysis. Notably, a highly active high-loading Fe-GY catalyst is identified, exhibiting an ultralow overpotential of 0.39 V. Furthermore, mechanistic analysis reveals that synergistic interactions between adjacent Fe atoms in high-loading Fe-GY reshape the local charge distribution. This electronic modulation optimizes both the Fe–O bonding and Fe 3d orbital characteristics, thereby enhancing intermediate binding and boosting OER activity. We believe that these findings provide valuable insights for accelerating the development of highly active, high-loading SACs.

Computational methods

All spin polarization calculations were performed using the Vienna *Ab initio* Simulation Package periodic density functional theory (DFT) approach.[21] The Perdew–Burke–Ernzerhof functional in the generalized gradient approximation was used to describe the exchange–correlation potential energy.[22] For calculations on Fe, Co, Ni, Cu, Rh, Pd, Ag, Ir, and Pt systems, the GGA + U method was applied to treat strong electron correlations in d-orbitals, using Hubbard *U* parameters of 5.0 eV (Fe), 6.3 eV (Co), 6.4 eV (Ni), 7.2 eV (Cu), 3.7 eV (Rh), 1.7 eV (Pd), 1.6 eV (Ag), 1.4 eV (Ir), and 1.7 eV (Pt).[18,23] Wave functions were accurately represented using the projector augmented wave approach, implemented with a plane wave basis set at a kinetic energy cut-off of 500 eV.[24] GY surface simulations employed a $2 \times 2 \times 1$ supercell with a 15 Å vacuum layer to prevent interslab interactions, using the DFT-D3 method for van der Waals corrections.[25] For geometric relaxation and electronic structure calculations, Γ-centered grids of $2 \times 2 \times 1$ and $9 \times 9 \times 1$ were utilized to sample the surface Brillouin zone, respectively. The convergence threshold for the total energy is set to 1×10^{-5} eV, and the forces on each atom during ionic relaxation must be below 0.02 eV $Å^{-1}$.

Results and discussion

In this work, the structural properties of GY critically influence the catalytic process. Consequently, Fig. 2a presents detailed geometric parameters of the optimized pristine GY unit cell. We employed a $2 \times 2 \times 1$ GY supercell for calculations, where the lattice constant of the primitive cell (indicated by dashed lines) is 6.89 Å, demonstrating excellent agreement with theoretical values.[26] The unit cell of GY contains 12 carbon atoms that are either sp-hybridized or sp^2-hybridized. GY therefore exhibits three types of C–C bonds: sp^2–sp^2 (1.42 Å), sp–sp (1.22 Å), and sp^2–sp (1.41 Å), which aligns with previously reported data.[19,20] Additionally, this structure exhibits naturally distributed porous cavities and other distinctive physical and chemical properties, as illustrated in Fig. 1a.

In principle, all 3d, 4d, and 5d TMs can form TM-GY. However, Talib *et al.* have comprehensively studied the OER activity of low-loading TM-GY, identifying low-loading Fe-, Co-, Ni-, Cu-, Rh-, Pd-, Ag-, Ir-, and Pt-GY exhibiting relatively low overpotentials (0.46 V to 1.20 V).[20] Given that high loading has a limited effect on overpotential, only these nine TMs were studied. We first determine the adsorption sites of these TM atoms on GY. For multiple binding sites, including positions above the C6 ring, above the C–C bond, above the C atom, and in the H cavity, literature shows that the metal preferentially adsorbs above the H cavity and binds to six sp-hybridized carbon atoms.[19,20] Moreover, a large hexagonal ring formed by six H cavities surrounding a benzene ring replaces the structure shown in Fig. 2a to represent the GY surface. The cavities are labeled H_1 to H_4 as illustrated in Fig. 2b. We propose that the configuration

TM	3d	Sc	Ti	V	Cr	Mn	Fe	Co	Ni	Cu	Zn
	4d	Y	Zr	Nb	Mo	Tc	Ru	Rh	Pd	Ag	Cd
	5d	La-Lu	Hf	Ta	W	Re	Os	Ir	Pt	Au	Hg

Fig. 1 The transition metals examined in the present work.

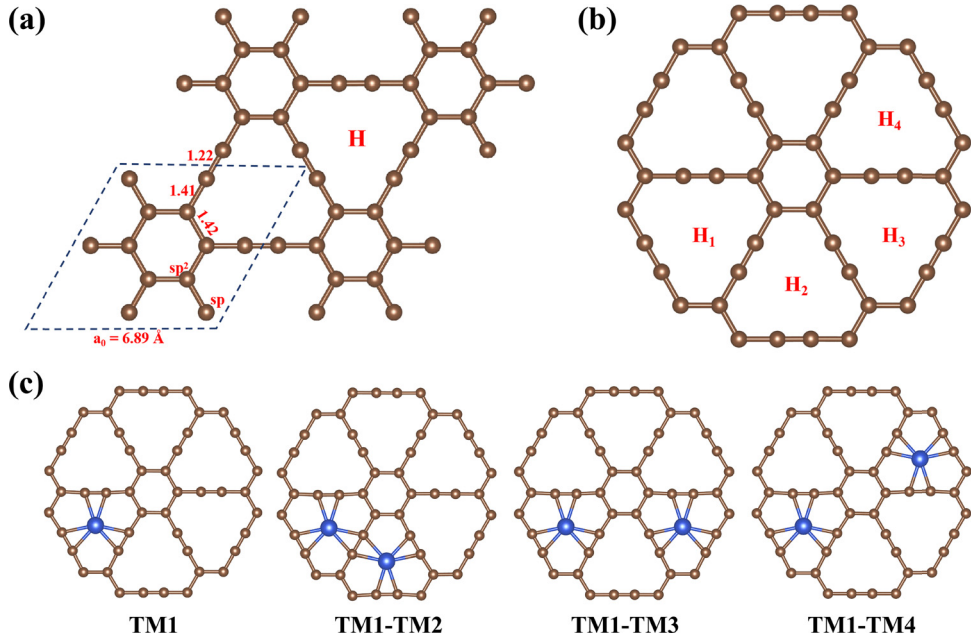

Fig. 2 (a) Optimized atomic structure of the unmodified 2 × 2 × 1 GY supercell, where dotted lines depict the original GY units. (b) Atomic structure of the GY framework for subsequent display of all structures. (c) Atomic structures of low-loading (TM1) and high-loading TM-GY (TM1–TM2, TM1–TM3, TM1–TM4). The numerals 1–4 denote the TM site labeling, corresponding to cavities H_1–H_4.

formed by binding a single TM atom to the H_1 cavity of GY corresponds to low-load TM-GY, designated as TM1. Building upon low-load TM-GY, we constructed high-load TM-GY configurations by introducing a second TM atom. This additional atom may adsorb at $H_2/H_3/H_4$ sites, yielding three distinct configurations: TM1–TM2, TM1–TM3, and TM1–TM4, as shown in Fig. 2c.

Before investigating the catalytic activity of the OER, the stability of TM atoms embedded in GY must be assessed. The low-loading TM-GY has only one configuration (TM1), and its structures are shown in Fig. S2. To determine the most stable configuration of the high-loading TM-GY, we calculated and compared the energies of three possible configurations. As highlighted in red in Table S1, the most stable configurations for high-loading Fe-GY and Pd-GY are TM1–TM3, while for Co-, Ni-, Cu-, Rh-, Ag-, Ir-, and Pt-GY are TM1–TM4. The corresponding optimized structures are illustrated in Fig. S3. Notably, the TM1–TM2 configuration was absent in the studied metals, likely because this structure requires two metal atoms to share two sp-hybridized carbon atoms, destabilizing the system. Fig. 3a and b present the calculated binding energies between TM atoms and the GY surface. For both low-loading and high-loading TM-GY, the TM atom binding energies range from −0.65 to −3.83 eV and −0.57 to −3.92 eV, respectively, indicating strong binding between TM atoms and GY. Fig. 3a and b further quantify the clustering energies of TM atoms on GY, illustrating aggregation propensity, while Fig. S4 presents the adsorption configurations of a TM dimer on GY. Among all TM-GY, TM atoms exhibit negative clustering energies in all cases except low-loading Pd-GY and both low- and high-loading Ag-GY, indicating high dispersion tendencies for the remaining catalysts. In summary, GY serves as an effective carrier for the TM SACs studied here, with the exception of these three material types. Consequently, these exceptional cases will be excluded from subsequent catalytic investigations. Furthermore, the climb image

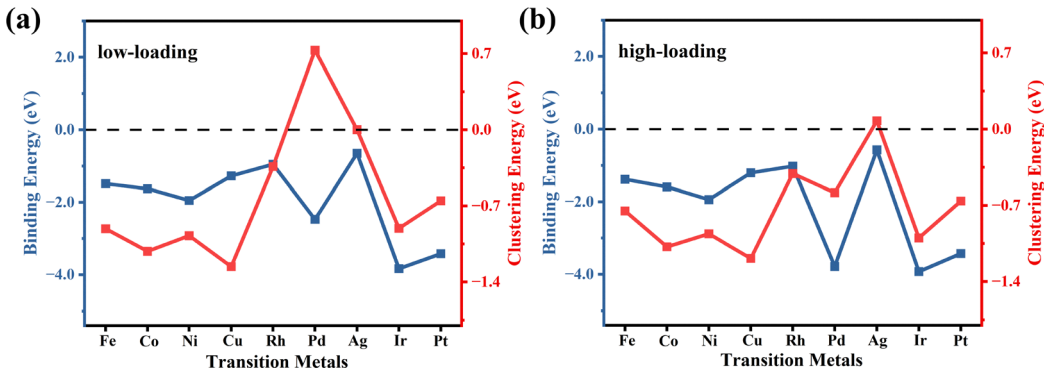

Fig. 3 Binding and clustering energies of TM atoms in (a) low-loading TM-GY and (b) high-loading TM-GY.

driven elastic band (Cl-NEB) method was employed to examine the possibility of Fe atom migration among the most stable adsorption sites in the Fe-GY catalyst. Two migration pathways were considered: diffusion between adjacent H cavities, and diffusion from an H cavity to a C6 cavity. As shown in Fig. S10, both the low- and high-loading Fe-GY exhibit high energy barriers for these processes, with values of 1.80 eV, 3.42 eV, 1.59 eV, and 1.60 eV, respectively. Since Fe atoms adsorbed in the C6 cavity are unstable in the high-loading case, the corresponding migration pathway was excluded from consideration. Therefore, the aggregation of adsorbed Fe atoms can be reliably ruled out.[27]

Subsequently, we performed a comprehensive investigation and comparison of the OER catalytic activity of TM-GY. The OER proceeds *via* four fundamental steps, as detailed in Fig. 4. Therefore, we calculated the free energy barrier for each step of every catalyst under acidic conditions (pH = 0) and determined the overpotential of all active sites using eqn (S6) in the SI, as shown in Fig. S5. In the figure, the low-loading TM-GY has only one metal site, whereas the high-loading TM-GY has two possible sites, which are labeled with numbers to indicate their identities. In addition, to more intuitively reflect the differences in catalyst activity between low and high loads, we presented the obtained overpotential data in a bar chart and highlighted the overpotential differences between the two load conditions, as shown in Fig. 5. For Fe and Co, the overpotential of TM-GY under high loading decreased by 0.64 and 0.13, respectively, relative to the low loading condition, indicating that increasing the loading can significantly enhance their OER catalytic activity. However, for Ni, Cu, Rh, Ir, and Pt, the overpotential difference in TM-GY between high and low loading is very small, ranging from −0.09 V to +0.01 V, indicating that increasing the loading has almost no effect on the catalytic activity of these TM-GY. Due to the instability of low-loading Pd-GY, the Pd-GY system is excluded from the current analysis. Notably, The high-loading Fe-GY catalyst exhibits significantly higher activity than other studied catalysts, with an overpotential of 0.39 V—superior to the commonly used IrO_2 (0.56 V).[28]

To reveal the origin of the high catalytic activity of high-loading Fe-GY, the Gibbs free energy barriers of both low- and high-loading Fe-GY were first analyzed. As shown in Fig. 6a, at U = 0 V and pH = 0, both low- and high-loading Fe-GY exhibit the same trend: all reaction steps are energetically uphill. However, compared to the low-loading Fe-GY, the high-loading Fe-GY exhibits a more uniform intermediate free energy distribution. This significantly reduces the energy barrier of the rate-determining step (RDS) for the *OH → *O conversion from 2.25 eV to 1.63 eV (site 1)/1.62 eV (site 3), with the corresponding overpotential decreasing from 1.02 V to 0.40 V/0.39 V. Furthermore, the free energy diagrams of sites 1 and 3 nearly overlap, indicating that the two sites are equivalent. This equivalence arises because the chemical environments of the two metal sites in the TM1–TM3 configuration are identical, as demonstrated in Fig. 2c. Therefore, only site 3 with lower overpotential was considered in subsequent studies.

Changes in the OER activity of a catalyst often result from alterations in the binding strength between oxygen-containing intermediates and the catalyst. Fig. 6b displays the adsorption energies of oxygen-containing intermediates on low- and high-loading Fe-GY. As the Fe loading increases, the adsorption energies of *O and *OOH become more negative, while that of *OH becomes less negative. Consequently, the adsorption of O and OOH on the catalyst strengthens, whereas the adsorption of OH weakens. Relative to low-loading Fe-GY, the high-loading Fe-GY demonstrates optimized adsorption behavior that equalizes intermediate free energies, thereby substantially reducing overpotential, consistent with our previous analysis. Focusing on the RDS for the high-loading Fe-GY, the overpotential reduction stems from enhanced O adsorption and weakened OH adsorption.

To further reveal the origin of the high activity, we introduce the bonding and anti-bonding orbitals stable electron intensity difference (BASED) theory, applying it to analyze bonding/anti-bonding states and elucidate O/OH–TM bonding interactions.[29] Qiao *et al.* developed the BASED theory by integrating D-band center, Crystal Orbital Hamilton Population (COHP), and Molecular Orbital (MO) theory to establish a generalized descriptor for quantifying adsorption intensity, expressed as

$$\begin{aligned}\mathrm{BASED} &= \int_{-\infty}^{0} \varepsilon \times \mathrm{COHP}_{\mathrm{bond}}(\varepsilon)\mathrm{d}\varepsilon + \int_{-\infty}^{0} \varepsilon \times \mathrm{COHP}_{\mathrm{anti}}(\varepsilon)\mathrm{d}\varepsilon \\ &= \frac{\int_{-\infty}^{0}\varepsilon \times \mathrm{COHP}_{\mathrm{bond}}(\varepsilon)\mathrm{d}\varepsilon}{\int_{-\infty}^{0}\mathrm{COHP}_{\mathrm{bond}}(\varepsilon)\mathrm{d}\varepsilon} \times \int_{-\infty}^{0} \mathrm{COHP}_{\mathrm{bond}}(\varepsilon)\mathrm{d}\varepsilon \\ &\quad + \frac{\int_{-\infty}^{0}\varepsilon \times \mathrm{COHP}_{\mathrm{anti}}(\varepsilon)\mathrm{d}\varepsilon}{\int_{-\infty}^{0}\mathrm{COHP}_{\mathrm{anti}}(\varepsilon)\mathrm{d}\varepsilon} \times \int_{-\infty}^{0} \mathrm{COHP}_{\mathrm{anti}}(\varepsilon)\mathrm{d}\varepsilon \\ &= \varepsilon_{\mathrm{bond}} \times \mathrm{ICOHP}_{\mathrm{bond}} + \varepsilon_{\mathrm{anti}} \times \mathrm{ICOHP}_{\mathrm{anti}}\end{aligned}$$

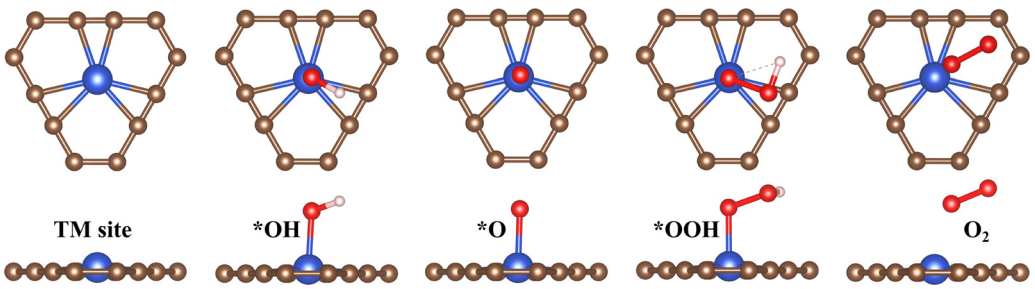

Fig. 4 Schematic illustration of the OER mechanism on the TM-GY material, where * denotes the TM site.

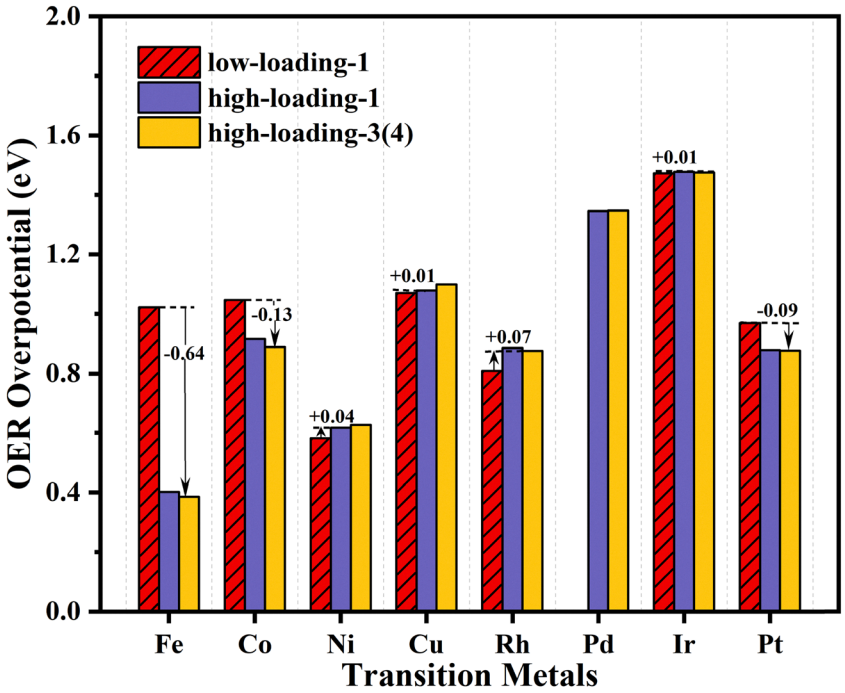

Fig. 5 OER overpotential differences between low- and high-loading TM-GY. The numerals 1, 3 and 4 denote the TM site labeling.

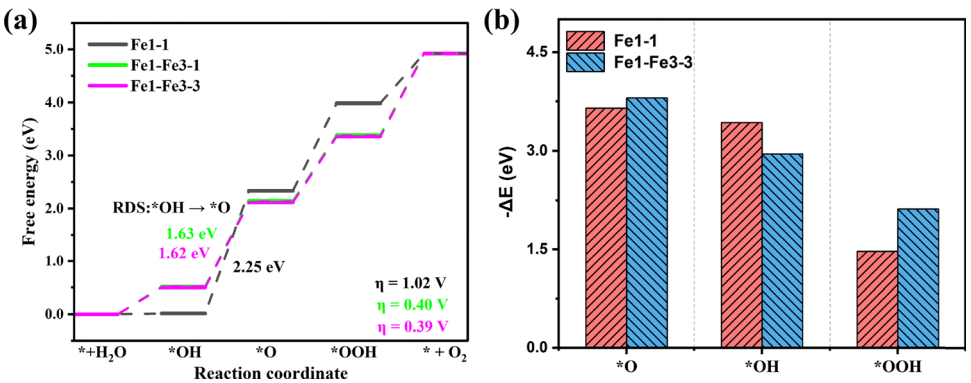

Fig. 6 (a) Free energy diagrams of low- and high-loading Fe-GY. (b) Adsorption energies of oxygen-containing intermediates on Fe1-1 and Fe1–Fe3-3 sites. The numerals 1 and 3 denote the TM site labeling.

where $COHP_{bond}$ (ε) and $COHP_{anti}$ (ε) represent COHP proportions of bonding and anti-bonding orbitals. $ICOHP_{bond}$ and $ICOHP_{anti}$ represent COHP integrals for bonding orbitals and anti-bonding orbitals. ε_{bond} and ε_{anti} represent the energy level centers of the bonding and anti-bonding orbitals, respectively. The BASED value represents the difference between the products of electrons' energy and their corresponding orbital energy level of electrons in bonding orbitals and anti-bonding orbitals. Therefore, it represents the strength of the formed bond, with a larger BASED value indicating a stronger bond. For *O on low- and high-loading Fe-GY, we computed the COHP between Fe and O atoms, yielding $ICOHP_{bond}$, $ICOHP_{anti}$, ε_{bond}, ε_{anti} and BASED values, shown in Fig. 7a and Table 1. Fig. S7(a and b) displays the optimized structures of O intermediates. The high-loading BASED increased from 8.52 eV^2 to 9.03 eV^2 compared with the low-loading BASED, indicating that the high-loading Fe sites exhibit enhanced binding with O. This observation is consistent with the calculated decrease in *O adsorption energy. Table 1 shows that the increase in BASED is primarily due to a significant increase in $|ICOHP_{bond}|$. We employed charge density difference and Bader charge calculations to investigate electron transfer in O adsorbed on both low- and high-loading Fe sites, as shown in Fig. 7(c and d). Compared to low loading, high loading increases electron transfer from Fe sites to O from 0.64 e to 0.70 e without altering the shapes of charge dissipation/accumulation regions, indicating enhanced electron involvement in Fe–O bond and a consequent rise in $|ICOHP_{bond}|$. Similarly, for *OH on low- and high-

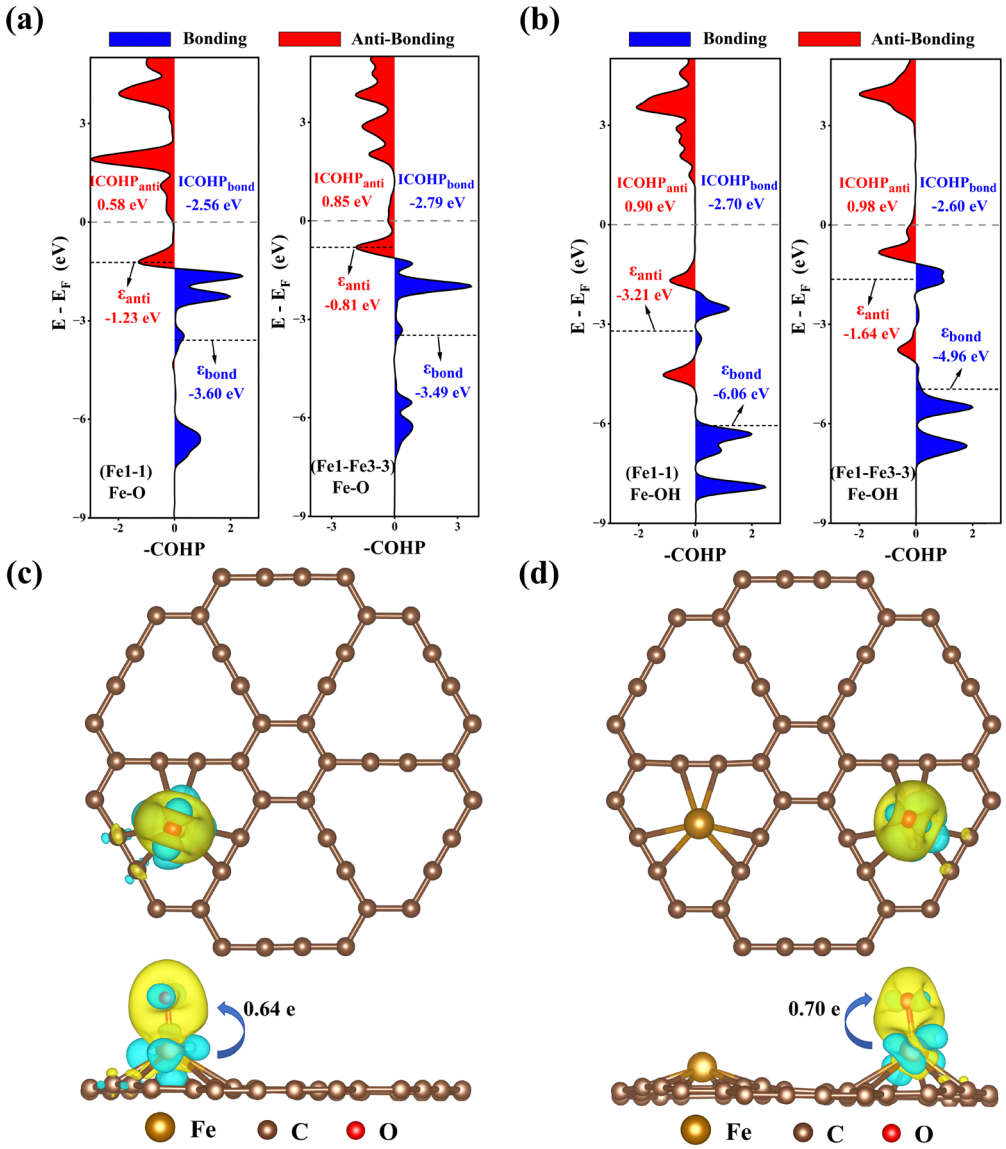

Fig. 7 COHP analysis of Fe–O bonding at (a) *O and (b) *OH in Fe1-1 and Fe1–Fe3-3 configurations. Charge differential density and Bader charge of O adsorbed on (c) Fe1-1 and (d) Fe1–Fe3-3 with an isosurface of 0.004 e Å^{-3}, where the loss of electrons is shown in blue and electron enrichment is shown in yellow. The numerals 1 and 3 denote the TM site labeling.

Table 1 ICOHP$_{bond}$, ICOHP$_{anti}$, ε_{bond}, ε_{anti}, and BASED values for Fe–O/OH bonds derived from the COHP. Numerals 1 and 3 denote the TM site labeling

	ICOHP$_{bond}$ (eV)	ε_{bond} (eV)	ICOHP$_{anti}$ (eV)	ε_{anti} (eV)	BASED (eV^2)
(Fe1-1)Fe–O	−2.56	−3.60	0.58	−1.23	8.52
(Fe1–Fe3-3)Fe–O	−2.79	−3.49	0.85	−0.81	9.03
(Fe1-1)Fe–OH	−2.70	−6.06	0.90	−3.21	13.49
(Fe1–Fe3-3)Fe–OH	−2.60	−4.96	0.98	−1.64	11.28

loading Fe-GY, we calculated the COHP between Fe and O atoms and associated parameters, as shown in Fig. 7b and Table 1. The high-loading BASED decreased from 13.49 eV^2 to 11.28 eV^2 compared with the low-loading BASED, indicating that the Fe sites under high loading have weaker binding with OH, which is consistent with the calculated increase in *OH adsorption energy. However, unlike the case for *O, the reduction in *BASED* for high-loading *OH mainly stems from an upshift in its ε_{bond} and ε_{anti}. In fact, the ε_{bond} and ε_{anti} of high-loading *O also undergo the same change, as shown in Table 1.

This variation stems from significant modulation of the Fe 3d projected density of states (PDOS) under high-loading condition. Fig. 8(a and b) show the Fe 3d PDOS of low- and high-loading Fe-GY, and respectively contain the O 2p PDOS of O free radical (Fig. 8a) and OH free radical (Fig. 8b). The contribution of O 2s is negligible. Furthermore, corroborated by spin-polarized COHP analysis in Fig. S6, we deduce: In the spin-up PDOS, the Fe 3d state exhibits continuous distributions at both low- and high-loading Fe-GY, with the d-band center upshifting from −4.97 eV at low loading to −4.41 eV at high loading.

Consequently, the bonding and anti-bonding orbitals formed by Fe sites and O/OH free radical at high loading also shift to higher energies, as displayed in Fig. 7(a and b). However, the spin-down PDOS for Fe 3d orbitals is discontinuous, with the region near the Fermi-level playing a key role in bonding. The spin-down Fe 3d PDOS of low-loading Fe-GY has two distinct peaks at the Fermi-level that strongly couple with nearby O/OH states to form bonding orbitals at lower energies (anti-bonding orbital is disregarded). In the high-loading Fe-GY, the energy levels of these two peaks decrease to around −1.8 eV. Therefore, the Fe–O/OH coupling weakens, and the formed bonding orbitals upshift, as shown in Fig. 7(a and b). Conclusively, modifications in the spin-polarized Fe 3d PDOS of high-loading Fe-GY drive an upshift in both ε_{bond} and ε_{anti}.

Fundamentally, both the altered electron transfer at Fe–O and modified Fe 3d PDOS in high-loading Fe-GY originate from synergistic interactions between adjacent metal centers. The charge density difference and Bader charge between Fe atoms and the GY were calculated for low- and high-loading Fe-GY to investigate charge transfer and redistribution, as shown in Fig. 8(c and d). Fig. S7(c and d) displays the optimized structures of Fe-GY. Compared to the low-loading, the number of electrons transferred from Fe atoms to GY in the high-loading Fe-GY remained largely unchanged (0.76 e → 0.75 e). However, distortion occurred in the charge accumulation and depletion regions around Fe sites, signifying synergistic interactions between adjacent Fe atoms in the high-loading Fe-GY. This interatomic interaction ultimately reshaped the local charge distribution around Fe centers. This directly or indirectly affects charge transfer during subsequent adsorption of oxygen-containing intermediates. Moreover, charge distribution is intrinsically linked to the density of states (DOS), which characterizes electronic state distribution. Consequently, alteration in charge distribution ultimately modify the Fe 3d PDOS. In addition, Fig. S8

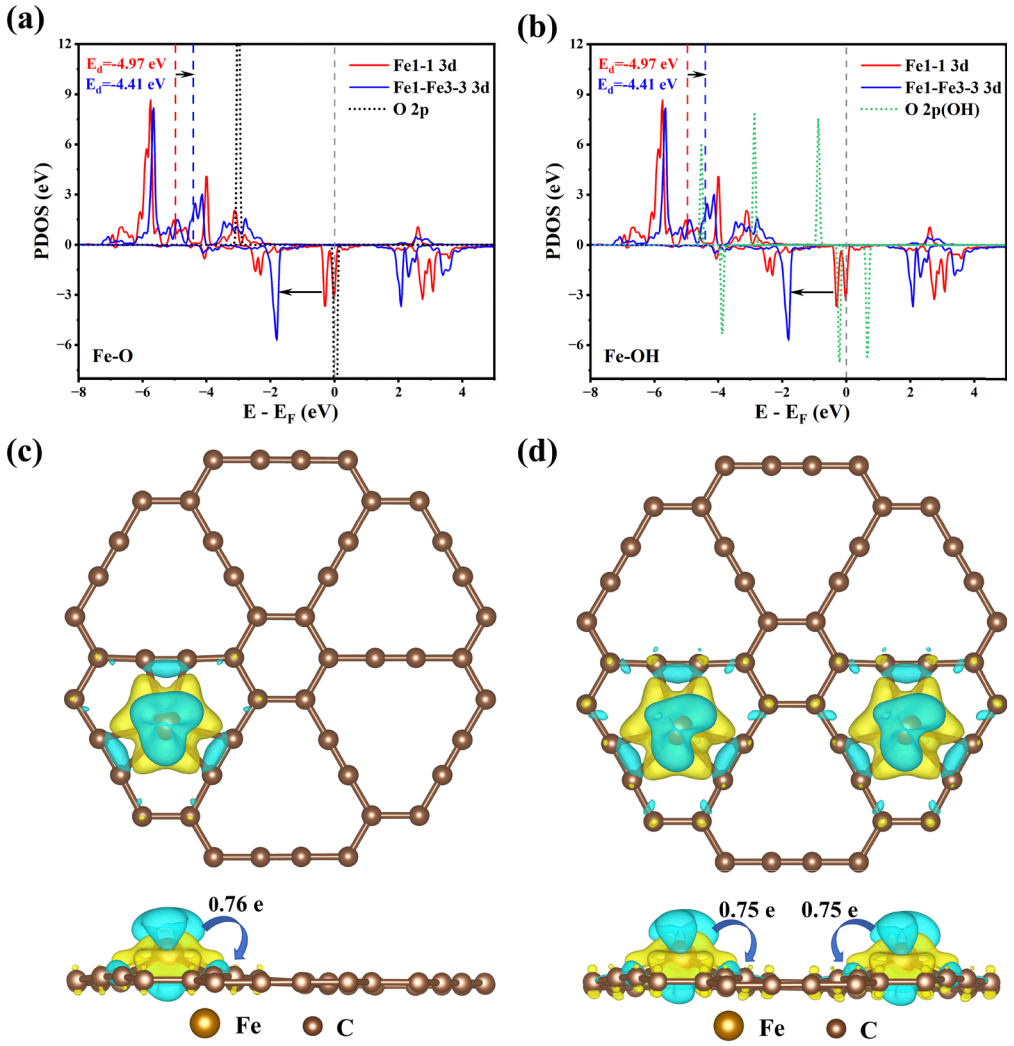

Fig. 8 (a) Projected density of states: Fe1-1 3d (red), Fe1–Fe3-3 3d (blue), and O 2p of O free radical (black). (b) Projected density of states: Fe1-1 3d (red), Fe1–Fe3-3 3d (blue), and O 2p of OH free radical (green). Charge difference density for Fe adsorbed on GY with an isosurface of 0.005 e Å^{-3}: (c) low-loading and (d) High-loading Fe-GY. The loss of electrons is shown in blue and electron enrichment is shown in yellow. The numerals 1 and 3 denote the TM site labeling.

presents the DOS of the six carbon atoms within the H1 hole in pure GY, the DOS of the six carbon atoms within the H3 hole in the Fe1 structure, and the 3d PDOS of the Fe atom (corresponding carbon atomic positions are illustrated in Fig. S7). A noticeable change is observed in the DOS of the Fe1–H3 compared to that of GY-H1. This indicates that the synergistic interaction between adjacent metal centers alters the bonding between the H3 hole and the iron atoms, ultimately leading to changes in the electronic properties of Fe1–Fe3.

Conclusions

In summary, we systematically assessed metal-binding characteristics and OER activities across nine TM-GY systems (TM = Fe, Co, Ni, Cu, Rh, Pd, Ag, Ir, and Pt) under both high- and low-loading conditions, elucidating the loading-activity relationship and screening optimal catalyst. Binding energy and clustering energy data demonstrate that, while Pd is not adsorbed at low loading and Ag is not adsorbed at all, other metals can stably anchor on GY at both low and high loading. In high-loading TM-GY, Fe and Pd adopt TM1–TM3 configuration, while other transition metals stabilize at TM1–TM4 configuration. The comparison of overpotentials between low- and high-loading catalysts indicates that high loading reduces the overpotentials of Fe- and Cu-GY, while having almost no effect on those of other TM-GY catalysts (excluding Ag-GY and Pd-GY systems). Furthermore, a highly active catalyst—high-loading Fe-GY—with an overpotential of only 0.39 V is identified. Finally, the origin of the high activity in the high-loading Fe-GY was investigated. Compared to low-loading Fe-GY, high-loading Fe-GY reshapes the charge distribution at Fe sites through synergistic interactions between adjacent Fe atoms. This modification alters both the electron transfer within Fe–O and the Fe 3d PDOS, thereby optimizing the binding strength and free energy of oxygen-containing intermediates and enhancing the OER activity.

Author contributions

D. Zhang made computational calculations and wrote the original draft. L. Xie conceived the experiments, review & editing the writing. Q. Lin, G. Nan, Y. Zhang and D. Fu assisted in completing the experiment. All the authors approved the final manuscript.

Conflicts of interest

The authors declare no conflict of interest.

Data availability

The data supporting the findings of this study are available within the article and its supplementary information (SI). Supplementary information is available. See DOI: https://doi.org/10.1039/d6cp00014b.

Acknowledgements

We are thankful for the financial support from the Zhejiang Provincial Natural Science Foundation Youth Fund Project (Grant No. LQN26B030004) and the Central Zhejiang Science and Technology Innovation Corridor Joint Fund of Zhejiang Provincial Natural Science Foundation of China (Grant No. LJHSD26A050001).

Notes and references

1 X. X. Shi, Z. L. Wen, Q. Q. Gu, L. Jiao, H. L. Jiang, H. F. Lv, H. W. Wang, J. N. Ding, M. P. Lyons and A. Chang, *et al.*, Metal-support frontier orbital interactions in single-atom catalysis, *Nature*, 2025, **640**, 668–675.
2 M. Chen, Y.-J. Zhao, J.-H. Liao and X.-B. Yang, Transition-metal dispersion on carbon-doped boron nitride nanostructures: Applications for high-capacity hydrogen storage, *Phys. Rev. B:Condens. Matter Mater. Phys.*, 2012, **86**, 045459.
3 J. M. Luo, Y. T. Zhang, Z. Lu, C. Liu, Y. S. Xu, H. Chen, Q. Wang, D. X. Wu, D. Dang and Y. J. Deng, *et al.*, Oxygen-Coordinated Cr Single-Atom Catalyst for Oxygen Reduction Reaction in Proton Exchange Membrane Fuel Cells, *Angew. Chem., Int. Ed.*, 2025, **64**, e202500500.
4 F. Jiang, Y. C. Li and Y. Pan, Design Principles of Single-Atom Catalysts for Oxygen Evolution Reaction: From Targeted Structures to Active Sites, *Adv. Mater.*, 2024, **36**, e2306309.
5 H. Y. Zhu, Y. J. Feng, D. S. Zheng, X. Y. Zhao, Y. Zhou, X. Y. Fu, L. Zhao and X. Chen, Theoretical prediction of emerging high-performance trifunctional ORR/OER/HER single-atom catalysts: transition metals anchored into pi-pi conjugated graphitic carbon nitride (g-C(10)N(3)), *Phys. Chem. Chem. Phys.*, 2023, **25**, 31983–31994.
6 R. Li, X. Y. Yan, M. Liu, Q. K. Zhao, J. Du, X. X. Tan, J. X. Ba, R. G. Zeng, W. H. Luo and J. S. Xu, Cathodic corrosion as a facile and universal method for scalable preparation of powdery single atom electrocatalysts, *Nano Res.*, 2024, **17**, 4943–4950.
7 Y. Han, Y. Wei, A. Goswami and A. Alexandrova, Uncovering the True Active Sites in Ni-N-C Catalysts for CO(2) Electroreduction, *J. Am. Chem. Soc.*, 2025, **147**, 38636–38646.
8 C. Gallagher, M. Kothakonda and Q. Zhao, Graphene-based single-atom catalysts for electrochemical CO(2) reduction: unraveling the roles of metals and dopants in tuning activity, *Phys. Chem. Chem. Phys.*, 2025, **27**, 5464–5475.
9 W. Zhang, D. Liu, T. Liu, C. L. Ding, T. Chen, Y. M. Li, X. K. Liu, L. Wang, C. L. Li and J. F. He, *et al.*, Coordinately unsaturated nickel single atom electrocatalyst for efficient CO2 conversion, *Nano Res.*, 2023, **16**, 10873–10880.
10 P. Kumar, K. Kannimuthu, A. S. Zeraati, S. Roy, X. Wang, X. Y. Wang, S. Samanta, K. A. Miller, M. Molina and D. Trivedi, *et al.*, High-Density Cobalt Single-Atom Catalysts for Enhanced Oxygen Evolution Reaction, *J. Am. Chem. Soc.*, 2023, **145**, 8052–8063.

11 Z. Chen, S. Zhang, J. Yang, C. Chen, Y. C. Song, C. L. Xu, M. Q. Wu and J. X. Liao, Rational design and controllable synthesis of polymer aerogel-based single-atom catalysts with high loading, *Mater. Adv.*, 2021, **2**, 6885–6900.
12 X. Gong, J. P. Bao, X. Wang, X. Wan, Y. H. Gu, C. Han, J. L. Shui, X. Z. Su, J. J. Ge and W. Xing, *et al.*, Dry-Solid-Electrochemical Synthesis: A General Method for Large Scale Synthesis of Single-Atom Catalysts with High Metal loadings, *Angew. Chem., Int. Ed.*, 2025, **64**, e202419374.
13 S. S. Li, W. Wang, H. Z. Wu, X. C. Wang, S. H. Ding, J. Y. Liu, X. W. Zhang, J. L. Sun, C. H. Fu and M. H. Zhou, Facile cascade-anchored synthesis of ultrahigh metal loading single-atom for significantly improved Fenton-like catalysis, *Nat. Commun.*, 2025, **16**, 8796.
14 J. Q. Shan, C. Ye, Y. L. Jiang, M. Jaroniec, Y. Zheng and S. Z. Qiao, Metal-metal interactions in correlated single-atom catalysts, *Sci. Adv.*, 2022, **8**, eabo0762.
15 H. Q. Jin, K. X. Zhou, R. X. Zhang, H. J. Cui, Y. Yu, P. X. Cui, W. G. Song and C. Y. Cao, Regulating the electronic structure through charge redistribution in dense single-atom catalysts for enhanced alkene epoxidation, *Nat. Commun.*, 2023, **14**, 2494.
16 Z. Y. Jin, P. P. Li, Y. Meng, Z. W. Fang, D. Xiao and G. H. Yu, Understanding the inter-site distance effect in single-atom catalysts for oxygen electroreduction, *Nat. Catal.*, 2021, **4**, 615–622.
17 L. L. Wu, Q. D. Li, C. F. Yang, X. Q. Ma, Z. F. Zhang and X. L. Cui, Constructing a novel TiO2/γ-graphyne heterojunction for enhanced photocatalytic hydrogen evolution, *J. Mater. Chem. A*, 2018, **6**, 20947–20955.
18 J. J. He, S. Y. Ma, P. Zhou, C. X. Zhang, C. Y. He and L. Z. Sun, Magnetic Properties of Single Transition-Metal Atom Absorbed Graphdiyne and Graphyne Sheet from DFT+U Calculations, *J. Phys. Chem. C*, 2012, **116**, 26313–26321.
19 S.-L. Li, Q. Li, Y. T. Chen, Y. Zhao and L.-Y. Gan, Transition metal embedded graphynes as advanced bifunctional single atom catalysts for oxygen reduction and evolution reactions, *Appl. Surf. Sci.*, 2022, **605**, 154828.
20 S. H. Talib, B. Bashir, M. A. Khan, B. Ali, S. Mohamed, A. Qurashi and J. Li, Improving the Efficiency of Water Splitting and Oxygen Reduction Via Single-Atom Anchoring on Graphyne Support, *Energy Environ. Mater.*, 2024, **7**, e12723.
21 G. Kresse and J. Furthmüller, Efficiency of ab-initio total energy calculations for metals and semiconductors using a plane-wave basis set, *Comput. Mater. Sci.*, 1996, **6**, 15–50.
22 J. P. Perdew, K. Burke and M. Ernzerhof, Generalized Gradient Approximation Made Simple, *Phys. Rev. Lett.*, 1996, **77**, 3865–3868.
23 M. Cococcioni and S. de Gironcoli, Linear response approach to the calculation of the effective interaction parameters in theLDA + Umethod, *Phys. Rev. B:Condens. Matter Mater. Phys.*, 2005, **71**, 035105.
24 P. E. Blöchl, Projector augmented-wave method, *Phys. Rev. B:Condens. Matter Mater. Phys.*, 1994, **50**, 17953–17979.
25 S. Grimme, J. Antony, S. Ehrlich and H. Krieg, A consistent and accurate ab initio parametrization of density functional dispersion correction (DFT-D) for the 94 elements H-Pu, *J. Chem. Phys.*, 2010, **132**, 154104.
26 P. Wu, P. Du, H. Zhang and C. X. Cai, Graphyne-supported single Fe atom catalysts for CO oxidation, *Phys. Chem. Chem. Phys.*, 2015, **17**, 1441–1449.
27 X. P. Gao, Y. N. Zhou, Y. J. Tan, B. W. Yang, Z. W. Cheng and Z. M. Shen, Single Mo atoms supported on N-Doped carbon with N/C edge-site for enhanced electrochemical hydrogen evolution, *Int. J. Hydrogen Energy*, 2019, **44**, 14861–14868.
28 J. Rossmeisl, Z. W. Qu, H. Zhu, G. J. Kroes and J. K. Nørskov, Electrolysis of water on oxide surfaces, *J. Electroanal. Chem.*, 2007, **607**, 83–89.
29 Z. L. Qiao, R. Jiang, J. Yun and D. P. Cao, Why the abnormal phenomena of D-band center theory exist? A new BASED theory for surface catalysis and chemistry, *Chin. J. Catal.*, 2024, **64**, 44–53.